nature materials

ARTICLES

https://doi.org/10.1038/s41563-018-0108-3

Re-entrant charge order in overdoped $(Bi,Pb)_{2.12}Sr_{1.88}CuO_{6+\delta}$ outside the pseudogap regime

Y. Y. Peng[1,11], R. Fumagalli[1], Y. Ding[2], M. Minola[3], S. Caprara[4,5], D. Betto[6], M. Bluschke[3], G. M. De Luca[7,8], K. Kummer[6], E. Lefrançois[3], M. Salluzzo[8], H. Suzuki[3], M. Le Tacon[9], X. J. Zhou[2], N. B. Brookes[6], B. Keimer[3], L. Braicovich[1,6], M. Grilli[4,5] and G. Ghiringhelli[1,10*]

In the underdoped regime, the cuprate high-temperature superconductors exhibit a host of unusual collective phenomena, including unconventional spin and charge density modulations, Fermi surface reconstructions, and a pseudogap in various physical observables. Conversely, overdoped cuprates are generally regarded as conventional Fermi liquids possessing no collective electronic order. In partial contradiction to this widely held picture, we report resonant X-ray scattering measurements revealing incommensurate charge order reflections for overdoped $(Bi,Pb)_{2.12}Sr_{1.88}CuO_{6+\delta}$ (Bi2201), with correlation lengths of 40–60 lattice units, that persist up to temperatures of at least 250 K. The value of the charge order wavevector decreases with doping, in line with the extrapolation of the trend previously observed in underdoped Bi2201. In overdoped materials, however, charge order coexists with a single, unreconstructed Fermi surface without nesting or pseudogap features. The discovery of re-entrant charge order in Bi2201 thus calls for investigations in other cuprate families and for a reconsideration of theories that posit an essential relationship between these phenomena.

High-temperature superconductivity emerges upon doping of holes or electrons into Mott-insulating copper oxides. The strong electronic correlations responsible for Mott localization in the parent compounds generate various competing instabilities in the underdoped regime[1]. Although experiments have established charge order (CO) as a universal feature of moderately doped cuprates, its relationship to the ubiquitous 'pseudogap' phenomenon has been at the focus of several studies and is still unsettled. Early evidence of charge order had come from La-based cuprates, where charge 'stripes' were observed near the doping level $p = 1/8$ holes per Cu (refs [2–4]). More recently, resonant X-ray scattering (RXS) experiments revealed incommensurate charge order competing with superconductivity also in $YBa_2Cu_3O_{6+x}$ (Y123) and in Hg- and Bi-based cuprates[5–12]. A detailed comparison of the X-ray data against angle-resolved photoemission spectroscopy (ARPES) data on Bi-based cuprates[13] suggested that the onset temperature of CO is close to the pseudogap temperature T^*, and that its wavevector is comparable to the distance between the Fermi arc tips, therefore hinting at a link between CO and the pseudogap in hole-doped systems[14]. Also in Y123, the CO onset temperature appears always to be lower than T^*, whereas in electron-doped cuprates CO extends well above T^*, with an onset temperature close to that of the antiferromagnetic fluctuations, thus suggesting a possible connection between the two[15].

It is questioned to what extent CO competes or intertwines with superconductivity, because the phenomenology is still incomplete. When considering the doping p, it is commonly assumed that CO is present only up to the optimal level ($p \leq 0.16$), with the possible exception of overdoped $La_{2-x}Sr_xCuO_4$ (La214), where the observation by inelastic neutron scattering of incommensurate spin-order peaks up to $p = 0.25$ might be interpreted as indirect evidence of charge density modulations in a 'stripe' picture[16,17]. However, CO has not been directly observed in overdoped La214, and the locking of spin- and charge-modulations at high temperature in this family has been recently revised[18]. On the other hand, various instabilities have been predicted near the Lifshitz point in the overdoped regime[19–22], where a van Hove singularity (vHs) in the electronic density of states moves across the Fermi level and the geometry of the Fermi surface changes from 'hole-like' (that is, enclosing a region of empty states centred at the antiferromagnetic point) to 'electron-like' (that is, delimiting occupied states around the Γ point). The Bi2201 system is well suited to test these predictions, because the doping level can be tuned over a wide range, well into the overdoped regime, and it generates a single Fermi surface, at variance from bilayer compounds showing a double Fermi surface. The single Lifshitz point resulting from this electronic structure greatly facilitates the quantitative correlation between data generated by ARPES and RXS. Furthermore, the vHs is particularly strong due to the pronounced two-dimensional character of this system[23] with highly decoupled superconducting planes.

Here we present resonant inelastic X-ray scattering (RIXS) data that display sharp, intense incommensurate diffraction peaks in overdoped Bi2201 over a range of doping levels spanning the Lifshitz point and the endpoint of the superconducting dome. These peaks show properties similar to those of the charge density modulation signal in RXS observed in underdoped cuprates; therefore we assign them to CO. The continued decrease

[1]Dipartimento di Fisica, Politecnico di Milano, Milano, Italy. [2]Beijing National Laboratory for Condensed Matter Physics, Institute of Physics, Chinese Academy of Sciences, Beijing, China. [3]Max-Planck-Institut für Festkörperforschung, Stuttgart, Germany. [4]Dipartimento di Fisica, Università di Roma 'La Sapienza', Roma, Italy. [5]CNR-ISC, Roma, Italy. [6]ESRF, The European Synchrotron, Grenoble, France. [7]Dipartimento di Fisica 'E. Pancini', Università di Napoli Federico II, Napoli, Italy. [8]CNR-SPIN, Napoli, Italy. [9]Institute of Solid State Physics (IFP), Karlsruhe Institute of Technology, Karlsruhe, Germany. [10]CNR-SPIN, Dipartimento di Fisica, Politecnico di Milano, Milano, Italy. [11]Present address: Department of Physics and Seitz Materials Research Laboratory, University of Illinois, Urbana, IL, USA. *e-mail: giacomo.ghiringhelli@polimi.it

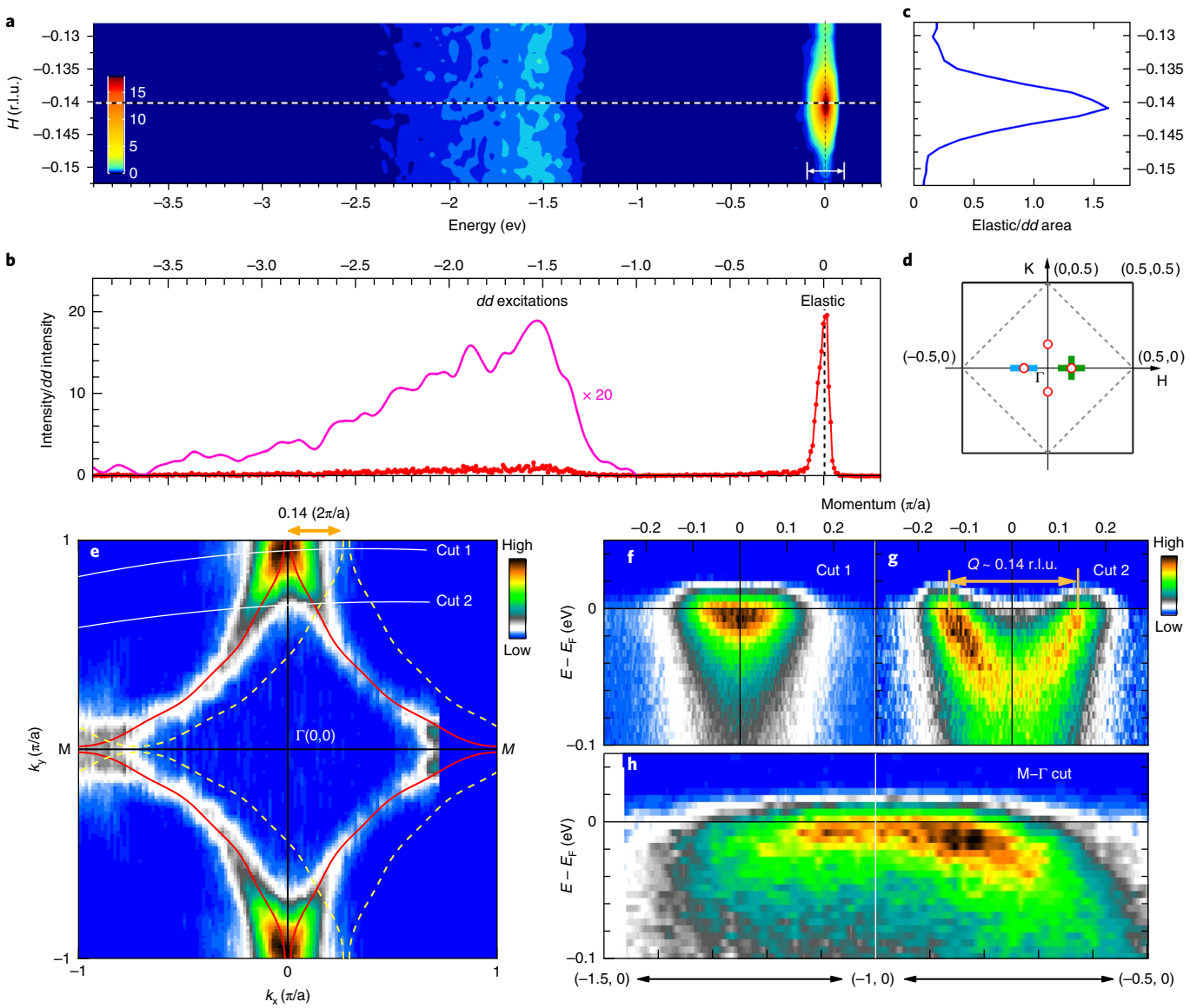

Fig. 1 | Observation of a quasi-elastic peak by RIXS in overdoped $(Bi,Pb)_{2.12}Sr_{1.88}CuO_{6+\delta}$ ($T_c = 11$ K, $p \sim 0.215$). **a**, Energy/momentum intensity map of RIXS spectra along the (−0.5,0)-(0,0) symmetry direction, indicated by the thick blue line in panel **d**. The data were taken with σ-polarized incident light at 20 K. **b**, The RIXS spectrum at $H \simeq -0.14$ r.l.u. indicated by the white dashed line shown in **a**. The *dd* excitations are shown additionally after smoothing and multiplied by 20 to be comparable to the elastic peak. **c**, The quasielastic RIXS intensity is given by the integral around $E \sim 0$, as indicated in **a**. **d**, Reciprocal-space image. The open red circles indicate the observed quasi-elastic peak. The thick blue line indicates the momentum cut for panel **a**, and the green cross indicates the momentum cuts for Fig. 2b. **e**, Photoemission intensity at the Fermi energy (E_F) as a function of momenta k_x and k_y for OD11K at 20 K. It is obtained by integrating within a (−10 meV, 10 meV) energy window and symmetrizing the original data with respect to the $(-\pi/a,0)$-$(\pi/a,0)$ line. The red lines, obtained by tight-binding fitting to the data, serve as a guide to the eyes. The dashed yellow lines indicate the Fermi surface shifted horizontally by $Q_{CO} \simeq 0.14$ r.l.u.. **f**, **g**, Electronic dispersions for the cuts (indicated by the white lines in **e**). **h**, Electronic dispersion for the cut along the M-Γ direction near the Brillouin zone boundary.

of the CO vector modulus versus increasing doping points to a picture where charge order would be ubiquitous across the entire phase diagram. Together with ARPES data on the same samples, our results provide experimental evidence at odds with models that posit an essential link between CO and the pseudogap. We performed RIXS measurements at the Cu L_3 edge on overdoped Bi2201 at four different doping levels (see Methods). We will hereafter use the common notations for the in-plane wavevector $\mathbf{Q}_\parallel$, the pseudo-tetragonal reciprocal lattice units (r.l.u.) $2\pi/a = 2\pi/b = 1$ (with $a \simeq b \simeq 3.83$ Å), and the reciprocal space indices (H,K,L). Figure 1a shows the energy/momentum intensity maps for OD11K ($T_c = 11$K, $p \sim 0.215$) along the H direction. The inelastic features in the [−3,−1] eV range, due to inter-orbital transitions (*dd* excitations)[24], depend weakly on momentum, whereas the response centred at zero energy loss exhibits a pronounced maximum at $\mathbf{Q}_\parallel = (-0.14, 0)$, shown in Fig. 1c. The RIXS spectrum at $H \simeq -0.14$ r.l.u. (Fig. 1b) is dominated by the elastic peak, which is approximately 20 times more intense than the *dd* excitations. We found the peak to be elastic within our experimental uncertainty (~10 meV), and will refer to this feature as a 'resonant elastic X-ray scattering' (REXS) peak.

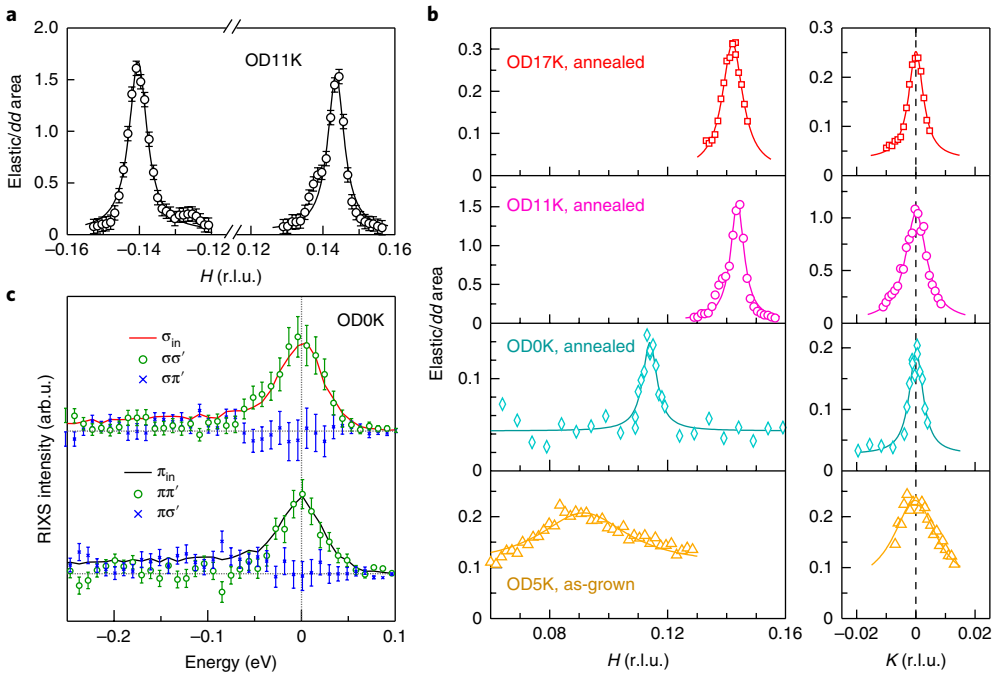

Fig. 2 | Doping and polarization dependence of the REXS peak in $(Bi,Pb)_{2.12}Sr_{1.88}CuO_{6+\delta}$. **a**, REXS intensity for positive and negative *H*, using σ polarization. **b**, *H* and *K* cuts at 20 K as indicated by the green cross in Fig. 1d, at four doping levels. Solid lines are Lorentzian peak fits to the data with a constant background. **c**, Polarization-resolved measurements for OD0K ($p \simeq 0.23$) taken at $H \simeq 0.115$ r.l.u. with incident π- and σ-polarized light. Statistical error bars are calculated from the number of counts (see Supplementary Information).

Figure 1e shows the Fermi surface (FS) of OD11K measured by ARPES at 20 K. We found no replicas of the large Fermi surface, and its shape offers no parallel segments suitable for a good nesting at the CO wavevector (0.14,0): the shifted FS exhibits a point-like crossing with the original one. In the antinodal region the band lies very close to the Fermi level energy (E_F), with no space for nesting (Fig. 1f). A cut through the FS points separated by $\mathbf{Q}_\parallel$ (Fig. 1g) shows no gap opening at E_F, which one would expect in a folded FS due to charge ordering[25]. On the other hand, a strong vHs is located slightly below E_F at the M point in the Brillouin zone boundary (Fig. 1h and Supplementary Fig. 7).

The REXS peak was found at both positive and negative *H* with similar intensity, as shown in Fig. 2a, and along both (1,0) and (0,1) directions. In contrast, we could not detect it along the (1,1) direction (Supplementary Fig. 9), in agreement with prior work on CO in underdoped cuprates[26,27]. Figure 2b provides the doping dependence of the REXS peak, with cuts along both *H* and *K* directions, as indicated by the green cross in Fig. 1d. It is important to note that three doping levels (OD17K, $p \sim 0.205$; OD11K, $p \sim 0.215$; OD0K, $T_c < 2$ K, $p \sim 0.23$) were obtained by post-annealing treatments of the as-grown OD5K ($p \sim 0.225$). Therefore, the latter is expected to have a higher degree of structural disorder, as confirmed by the much larger and anisotropic width of the REXS peak and by the broader superconducting transition (Supplementary Fig. 1a); moreover, the Q_{CO} value for OD5K falls outside the trend set by the three other samples.

To assess that the REXS peak arises from charge order, we exploited the polarimeter at our RIXS facility[28]. Spin-related scattering implies a 90° rotation of the photon polarization[29], whereas pure charge scattering, without spin-flip excitations, necessarily conserves the photon polarization. As shown in Fig. 2c, the REXS peak is purely polarization-conserving. To clarify whether the peak originates from a modulation of the valence electron charge density, we checked its resonant behaviour, since a charge density modulation is detectable only at resonance at our photon energy, whereas a generic lattice superstructure would be visible also off-resonance[30]. Figure 3a shows the incident photon energy dependence of the REXS peak, which closely resembles the spectra of the Cu L_3 x-ray absorption spectrum (XAS). Unlike YBCO, which has two inequivalent Cu sites contributing to the XAS spectra[6], in Bi2201 the Cu L_3 absorption peak is fully due to the Cu in the CuO_2 planes, and the strictly resonant peak can thus be unequivocally assigned to modulations of the charge density in the CuO_2 planes. Although the REXS peak intensity decreases upon detuning from the resonance, its position and width are unchanged (Fig. 3b). This photon energy dependence is identical to the resonance of CO in underdoped Bi2201 (ref. [13]).

Figure 3c shows the temperature dependence of the REXS peak in OD11K. Although the peak broadens slightly as the temperature is raised, its integrated intensity is almost independent of temperature up to 250 K (Fig. 3d), indicating that the onset of charge order occurs well above 250 K. Since T^* of OD11K is approximately zero[31], as confirmed by the absence of a gap at the antinode at 20 K (Fig. 1f), this means that the REXS peak is present in the absence of the pseudogap. The very small temperature dependence is confirmed by energy-integrated resonant X-ray scattering measurements, carried out on the OD17K sample (Fig. 3d and Supplementary Fig. 10), and showing that the REXS peak is invariant across T_c, similar to the CO behaviour in underdoped Bi2201 (ref. [13]). It is noteworthy that the competition between CO and superconductivity in the underdoped cuprates varies. Whereas the CO is found to compete prominently with superconductivity in underdoped Y123 (refs [6–10]) and La214 (ref. [32]), this behaviour is less evident in $Bi_2Sr_2CaCu_2O_{8+\delta}$ (ref. [33]), Bi2201 (refs [13,27]) and $HgBa_2CuO_{4+\delta}$ (refs [34,35]).

Figure 4 a–c presents an overview of the wavevector of the REXS peak, Q_{CO}, as well as its correlation length and its integrated intensity ('volume') as functions of doping, including earlier data on underdoped Bi2201 (refs [13,27]). The discovered Q_{CO} is approximately half of that of the underdoped samples, extending the known negative slope of Q_{CO} (*p*) to the overdoped region. As already mentioned, the peak intensity (normalized to the *dd* excitations) is

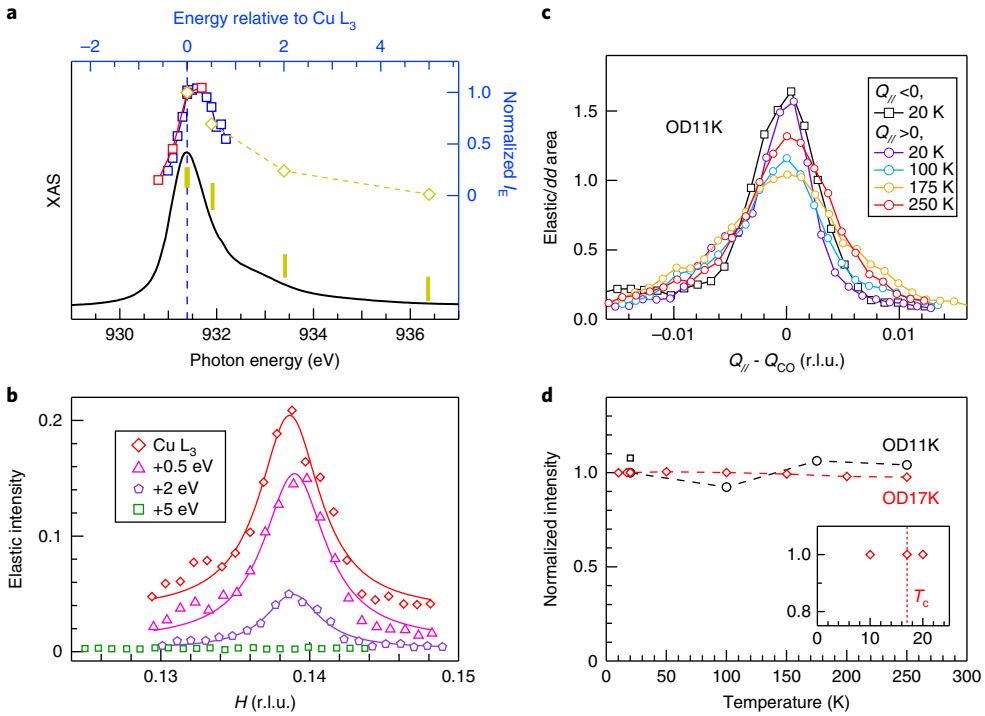

Fig. 3 | Energy and temperature dependence of the REXS peak in $(Bi,Pb)_{2.12}Sr_{1.88}CuO_{6+\delta}$. **a**, (Left and bottom axes) XAS spectra of OD17K with σ polarization at normal incidence. (Right and top axes) Incident energy dependence of the REXS intensity, normalized to the value at the XAS peak: open blue (red) squares for π (σ) polarization of OD11K, brown diamonds for σ polarization of OD17K. **b**, REXS scans along the *H* direction for OD17K at 20 K, at selected incident energies indicated by the brown lines in **a**. Solid lines are Lorentzian peak fits to the data with a constant background. **c**, Comparison of REXS scans at selected temperatures for OD11K with $Q_{CO} \simeq \pm 0.14$ (± 0.005) r.l.u.. **d**, Temperature dependence of the charge order intensity in OD11K and OD17K, normalized to the value at 20 K at $Q_{//}>0$. The inset zooms in on the low-temperature region around T_c for OD17K.

much higher in the overdoped samples. This is combined with a much smaller width in Q-space: the charge order is rather long-ranged in the overdoped region, with the only exception being the as-grown OD5K, whose REXS peak is relatively weak and broad. In the three other overdoped samples the correlation lengths $\xi_{H,K}$ are in the range from 40*a* to 60*a*, an order of magnitude larger than those of underdoped Bi2201 (~6*a*). It is noteworthy that this long-range correlation of charge order is comparable to the stripe-order in $La_{1.875}Ba_{0.125}CuO_4$ (refs [2–4]) and the field-induced CO in YBCO (refs [9,10]). Interestingly, the integrated intensity of the REXS peak (see Methods) also shows two comparable maxima, one around $p \sim 0.115$ and one around $p \sim 0.215$.

Figure 4d shows the extended phase diagram of charge order in Bi2201, including also the checkerboard-like charge order that was observed by scanning tunnelling microscopy (STM) from the insulating state ($p \simeq 0.07$)[36] up to OD15K ($p \simeq 0.21$)[37], and characterized by a doping-independent $Q_{CO} \sim 0.25$ r.l.u.. On the other hand, RXS measurements revealed a short-ranged CO in the pseudogap state up to optimal doping, and a long-ranged CO, with a small *T*-dependence between 20 K and 250 K, outside the pseudogap region up to $p \simeq 0.23$. Given the different charge order wavevectors determined from STM and RXS, their relations remain to be further studied. The schematic Fermi surfaces of Bi2201 at three selected dopings ($p \simeq 0.11$, 0.16 and 0.22) are shown on the top panels. A hole-like Fermi surface is observed in a broad doping range; it grows in size with doping and breaks into Fermi arcs below T^* (refs [38,39]). It eventually transforms into an electron-like FS in the case of OD0K, where the Lifshitz transition takes place in Bi2201 (ref. [39]).

Our discovery encourages a reconsideration of the charge ordering phenomenon and, with it, a reassessment of the theoretical models proposed so far. In particular, as spin instabilities have been reported only close to the Mott-insulating state, they are unlikely the cause of CO in the overdoped regime, where the vHs seems more relevant[19–22]. However, the instabilities related to the vHs are typically associated with nesting features of the Fermi surface that are absent in our experiments. Looking for an appealing common scenario for CO in underdoped and overdoped regions, we consider the 'frustrated phase separation' approach (see Methods and Supplementary Information), previously proposed for the underdoped regime[40–43], in which some generic (phononic and/or magnetic) non-critical effective attraction drives the system towards electronic phase separation. As the segregation of charges over large regions is prevented by the electron–electron Coulomb repulsion, the system finds a compromise by forming a CO state where charge is segregated on a short length scale while large-scale charge neutrality is maintained. This mechanism accounts for a ubiquitous tendency towards CO with a wavevector that is not tied to nesting features of the Fermi surface. It also accounts for a re-entrancy of charge order, because the propensity to this instability depends on the electronic density of states, which exhibits two maxima as a function of doping (Supplementary Fig. 12). The first maximum at low doping is due to narrowing of the conduction band induced by electronic correlations, and at high doping the vHs generates a second maximum.

In contrast to theories ascribing charge orders to antiferromagnetic correlations in the pseudogap phase, which are applicable only to the underdoped region[44–46], and to those that attribute charge instabilities only to the vHs, which are not relevant for CO in underdoped cuprates[20], we are suggesting here a unified scenario for the entire phase diagram. We note that alternative schemes[21,22] that rely on Fermi surface folding or nesting are difficult to reconcile with our ARPES results. Future work to address the detailed structural

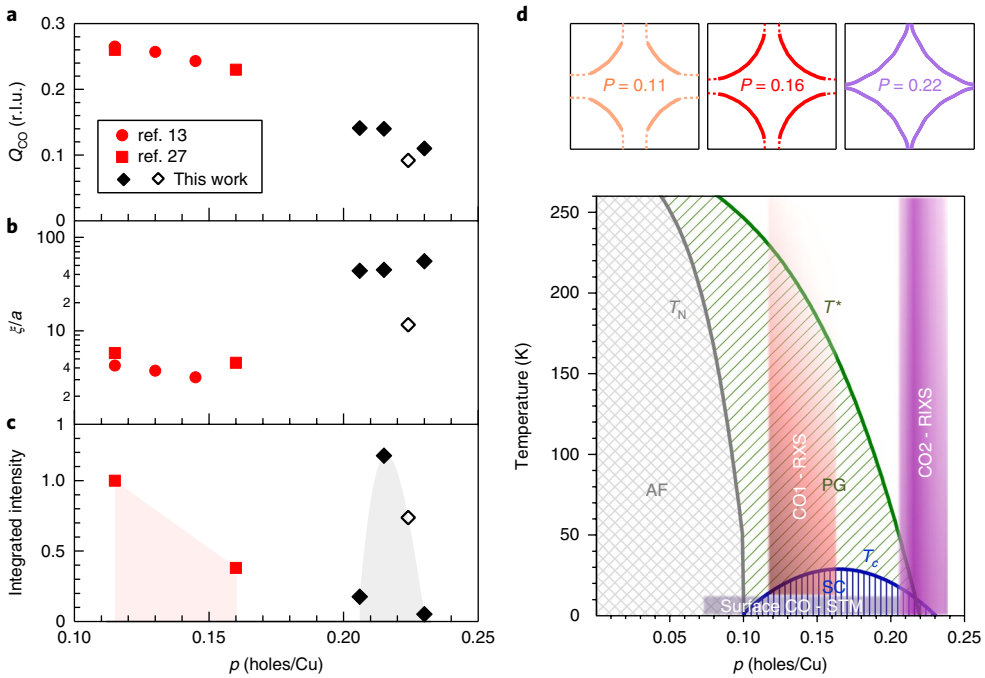

Fig. 4 | Doping dependence of the charge order signal in $(Bi,Pb)_{2.12}Sr_{1.88}CuO_{6+\delta}$ and the corresponding phase diagram. a–c, Doping dependence of the CO wavevector (**a**), correlation length (**b**) and the integrated intensity normalized to the value at $p \simeq 0.115$ (**c**). Data from RXS[13,27] are included; black diamonds for annealed (filled) and as-grown (open) samples. Error bars are smaller than the symbol dimensions. **d**, Phase diagram of the charge order in Bi2201: it shows the antiferromagnetic region (AF) defined by T_N, the superconducting region (SC) defined by T_c and the pseudogap region (PG) defined by T^*, which are reproduced from NMR measurements[31]. The grey shaded area denotes the checkerboard charge order observed with STM from $p = 0.07$ (ref. [36]) to $p = 0.21$ (ref. [37]); the red shaded area denotes the CO measured with X-rays[13,27]; the violet shaded area denotes the region of the discovered CO. The Fermi surfaces at selected doping $p = 0.11$, 0.16 and 0.22 are schematically depicted on the top panels, breaking into Fermi arcs at $T < T^*$.

and electronic textures of the CO state in Bi2201 is required to reveal the universality of CO in the overdoped regime. Although the vHs is generally observed in cuprates, its position and extent in momentum space strongly vary among families[47]. The study of other highly two-dimensional compounds such as the single-layer Tl-based cuprates can validate our interpretation. In any case, our discovery of a strong electronic instability in the overdoped regime invites an investigation of the commonalities and differences of cuprates across the optimal doping level and the nearby quantum critical points.

Methods

Methods, including statements of data availability and any associated accession codes and references, are available at https://doi.org/10.1038/s41563-018-0108-3.

Received: 17 August 2017; Accepted: 14 May 2018;
Published online: 11 June 2018

References

1. Keimer, B., Kivelson, S. A., Norman, M. R., Uchida, S. & Zaanen, J. From quantum matter to high-temperature superconductivity in copper oxides. *Nature* **518**, 179–186 (2015).
2. Tranquada, J. M., Sternlieb, B. J., Axe, J. D., Nakamura, Y. & Uchida, S. Evidence for stripe correlations of spins and holes in copper oxide superconductors. *Nature* **375**, 561–563 (1995).
3. Fujita, M., Goka, H., Yamada, K. & Matsuda, M. Competition between charge- and spin-density-wave order and superconductivity in $La_{1.875}Ba_{0.125-x}Sr_xCuO_4$. *Phys. Rev. Lett.* **88**, 167008 (2002).
4. Abbamonte, P. et al. Spatially modulated 'Mottness' in $La_{2-x}Ba_xCuO_4$. *Nat. Phys.* **1**, 155–158 (2005).
5. Wu, T. et al. Magnetic-field-induced charge-stripe order in the high-temperature superconductor $YBa_2Cu_3O_y$. *Nature* **477**, 191–194 (2011).
6. Ghiringhelli, G. et al. Long-range incommensurate charge fluctuations in $(Y,Nd)Ba_2Cu_3O_{6+x}$. *Science* **337**, 821–825 (2012).
7. Chang, J. et al. Direct observation of competition between superconductivity and charge density wave order in $YBa_2Cu_3O_{6.67}$. *Nat. Phys.* **8**, 871–876 (2012).
8. Blanco-Canosa, S. et al. Resonant X-ray scattering study of charge-density wave correlations in $YBa_2Cu_3O_{6+x}$. *Phys. Rev. B* **90**, 054513 (2014).
9. Gerber, S. et al. Three-dimensional charge density wave order in $YBa_2Cu_3O_{6.67}$ at high magnetic fields. *Science* **350**, 949–952 (2015).
10. Chang, J. et al. Magnetic field controlled charge density wave coupling in underdoped $YBa_2Cu_3O_{6+x}$. *Nat. Commun.* **7**, 11494 (2016).
11. Tabis, W. et al. Charge order and its connection with Fermi-liquid charge transport in a pristine high-T_c cuprate. *Nat. Commun.* **5**, 5875 (2014).
12. Hashimoto, M. et al. Direct observation of bulk charge modulations in optimally doped $Bi_{1.5}Pb_{0.6}Sr_{1.54}CaCu_2O_{8+\delta}$. *Phys. Rev. B* **89**, 220511(R) (2014).
13. Comin, R. et al. Charge order driven by Fermi-arc instability in $Bi_2Sr_{2-x}La_xCuO_{6+\delta}$. *Science* **343**, 390–392 (2014).
14. Allais, A., Chowdhury, D. & Sachdev, S. Connecting high-field quantum oscillations to zero-field electron spectral functions in the underdoped cuprates. *Nat. Commun.* **5**, 5771 (2014).
15. da Silva Neto, E. H. et al. Doping-dependent charge order correlations in electron-doped cuprates. *Sci. Adv.* **2**, 1600782 (2016).
16. Tranquada, J. M. et al. Coexistence of, and competition between, superconductivity and charge-stripe order in $La_{1.6-x}Nd_{0.4}Sr_xCuO_4$. *Phys. Rev. Lett.* **78**, 338–341 (1997).
17. Yamada, K. et al. Doping dependence of the spatially modulated dynamical spin correlations and the superconducting-transition temperature in $La_{2-x}Sr_xCuO_4$. *Phys. Rev. B* **57**, 6165–6172 (1998).
18. Miao, H. et al. High-temperature charge density wave correlations in $La_{1.875}Ba_{0.125}CuO_4$ without spin–charge locking. *Proc. Natl Acad. Sci. USA* **114**, 12430 (2017).
19. Zanchi, D. & Schulz, H. J. Superconducting instabilities of the non-half-filled Hubbard model in two dimensions. *Phys. Rev. B* **54**, 9509–9519 (1996).
20. Gonzalez, J. Charge instabilities near a van Hove singularity. *Phys. Rev. B* **63**, 045114 (2001).
21. Holder, T. & Metzner, W. Incommensurate nematic fluctuations in two-dimensional metals. *Phys. Rev. B* **85**, 165130 (2012).
22. Bulut, S., Atkinson, W. A. & Kampf, A. P. Spatially modulated electronic nematicity in the three-band model of cuprate superconductors. *Phys. Rev. B* **88**, 155132 (2013).

23. King, D. M. et al. Observation of a saddle-point singularity in $Bi_2(Sr_{0.97}Pr_{0.03})_2CuO_{6+\delta}$ and its implications for normal and superconducting state properties. *Phys. Rev. Lett.* **73**, 3298–3301 (1994).
24. Moretti Sala, M. et al. Energy and symmetry of *dd* excitations in undoped layered cuprates measured by Cu L_3 resonant inelastic X-ray scattering. *New J. Phys.* **13**, 043026 (2011).
25. Chen, C.-W., Choe, J. & Morosan, E. Charge density waves in strongly correlated electron systems. *Rep. Prog. Phys.* **79**, 084505 (2016).
26. Comin, R. et al. Symmetry of charge order in cuprates. *Nat. Mater.* **14**, 796–800 (2015).
27. Peng, Y. Y. et al. Direct observation of charge order in underdoped and optimally doped $Bi_2(Sr,La)_2CuO_{6+\delta}$ by resonant inelastic X-ray scattering. *Phys. Rev. B* **94**, 184511 (2016).
28. Braicovich, L. et al. The simultaneous measurement of energy and linear polarization of the scattered radiation in resonant inelastic soft X-ray scattering. *Rev. Sci. Instrum.* **85**, 115104 (2014).
29. Ament, L. J. P., Ghiringhelli, G., Moretti Sala, M., Braicovich, L. & van den Brink, J. Theoretical demonstration of how the dispersion of magnetic excitations in cuprate compounds can be determined using resonant inelastic X-ray scattering. *Phys. Rev. Lett.* **103**, 117003 (2009).
30. Abbamonte, P. Charge modulations versus strain waves in resonant X-ray scattering. *Phys. Rev. B* **74**, 195113 (2006).
31. Kawasaki, S. J. et al. Carrier-concentration dependence of the pseudogap ground state of superconducting $Bi_2Sr_{2-x}La_xCuO_{6+\delta}$ revealed by ^{63,65}Cu -nuclear magnetic resonance in very high magnetic fields. *Phys. Rev. Lett.* **105**, 137002 (2010).
32. Croft, T. P., Lester, C., Senn, M. S., Bombardi, A. & Hayden, S. M. Charge density wave fluctuations in $La_{2-x}Sr_xCuO_4$ and their competition with superconductivity. *Phys. Rev. B* **89**, 224513 (2014).
33. da Silva Neto, E. H. et al. Ubiquitous interplay between charge ordering and high-temperature superconductivity in cuprates. *Science* **343**, 393–396 (2014).
34. Tabis, W. et al. Synchrotron X-ray scattering study of charge-density-wave order in $HgBa_2CuO_{4+\delta}$. *Phys. Rev. B* **96**, 134510 (2017).
35. Campi, G. et al. Inhomogeneity of charge-density-wave order and quenched disorder in a high-T_c superconductor. *Nature* **525**, 359–362 (2015).
36. Cai, P. et al. Visualizing the evolution from the Mott insulator to a charge-ordered insulator in lightly doped cuprates. *Nat. Phys.* **12**, 1047–1052 (2016).
37. He, Y. et al. Fermi surface and pseudogap evolution in a cuprate superconductor. *Science* **344**, 608–611 (2014).
38. Meng, J. Q. et al. Coexistence of Fermi arcs and Fermi pockets in a high-T_c copper oxide superconductor. *Nature* **462**, 335–338 (2009).
39. Kondo, T. et al. Hole-concentration dependence of band structure in $(Bi,Pb)_2(Sr,La)_2CuO_{6+\delta}$ determined by the angle-resolved photoemission spectroscopy. *J. Electron Spectrosc. Relat. Phenom.* **137**, 663–668 (2004).
40. Emery, V. J. & Kivelson, S. A. Frustrated electronic phase separation and high-temperature superconductors. *Physica C* **209**, 597–621 (1993).
41. Castellani, C., Di Castro, C. & Grilli, M. Singular quasiparticle scattering in the proximity of charge instabilities. *Phys. Rev. Lett.* **75**, 4650–4653 (1995).
42. Andergassen, S., Caprara, S., Di Castro, C. & Grilli, M. Anomalous isotopic effect near the charge ordering quantum criticality. *Phys. Rev. Lett.* **87**, 056401 (2001).
43. Caprara, S., Di Castro, C., Seibold, G. & Grilli, M. Dynamical charge density waves rule the phase diagram of cuprates. *Phys. Rev. B* **95**, 224511 (2017).
44. Metlitski, M. A. & Sachdev, S. Quantum phase transitions of metals in two spatial dimensions. II Spin density wave order. *Phys. Rev. B* **82**, 075128 (2010).
45. Efetov, K. B., Meier, H. & Pépin, C. Pseudogap state near a quantum critical point. *Nat. Phys.* **9**, 442–445 (2013).
46. Wang, Y. & Chubukov, A. Charge-density-wave order with momentum (2*Q*,0) and (0,2*Q*) within the spin-fermion model: Continuous and discrete symmetry breaking, preemptive composite order, and relation to pseudogap in hole-doped cuprates. *Phys. Rev. B* **90**, 035149 (2014).
47. Markiewicz, R. S. A survey of the van Hove scenario for high-T_c superconductivity with special emphasis on pseudogaps and striped phases. *J. Phys. Chem. Sol.* **58**, 1179–1310 (1997).

Acknowledgements

This work was supported by ERC-P-ReXS project (2016-0790) of the Fondazione CARIPLO and Regione Lombardia, in Italy. M.M. was partially supported by the Alexander von Humboldt Foundation. X.J.Z. acknowledges financial support from the National Natural Science Foundation of China (11334010 and 11534007), the National Key Research and Development Program of China (2016YFA0300300) and the Strategic Priority Research Program (B) of Chinese Academy of Sciences (XDB07020300). S.C. and M.G. acknowledge financial support from the Sapienza University project no. C26A115HTN. M.S. and G.M.D.L. acknowledge funding from the project QUANTOX of QuantERA ERA-NET Cofund in Quantum Technologies implemented within the EU H2020 Programme. The authors acknowledge insightful discussions with T. P. Devereaux, S. Kivelson, C. Di Castro, B. Moritz, P. Abbamonte and W. Metzner. The authors acknowledge the help of S. Sun and P. Abbamonte for the X-ray diffraction measurements, collected at the Department of Physics and Seitz Materials Research Laboratory, University of Illinois, USA. The assistance of E. Schierle, for the RXS measurements at BESSY II (HZB), and of M. Celebrano, for the AFM images acquired at the Physics Department of the Politecnico di Milano, are gratefully acknowledged. The RIXS experimental data were collected at the beam line ID32 of the European Synchrotron (ESRF) in Grenoble (F) using the ERIXS spectrometer designed jointly by the ESRF and Politecnico di Milano.

Author contributions

G.G., Y.Y.P. and L.B. conceived and designed the experiments with suggestions from M.M., N.B.B. and B.K. Y.Y.P., R.F., G.G., L.B., M.M., D.B., G.M.D.L., K.K., E.L., M.S., H.S. and N.B.B. performed the RIXS measurements. M.M., R.F. and M.B performed the RXS measurements. G.G. contributed to AFM measurements. Y.D. and X.J.Z. performed the ARPES measurements. Y.Y.P. and G.G. analysed the RIXS experimental data. Y.Y.P., Y.D. and X.J.Z. analysed the ARPES experimental data. M.G. and S.C. performed the theoretical calculations. Y.D. and X.J.Z. synthesized, grew and characterized the Bi2201 single-crystals. Y.Y.P., G.G., B.K. and M.G. wrote the manuscript with the input from L.B., M.L.T., M.M. and R.F., and contributions from all authors.

Competing interests

The authors declare no competing interests.

Additional information

Supplementary information is available for this paper at https://doi.org/10.1038/s41563-018-0108-3.

Reprints and permissions information is available at www.nature.com/reprints.

Correspondence and requests for materials should be addressed to G.G.

Publisher's note: Springer Nature remains neutral with regard to jurisdictional claims in published maps and institutional affiliations.

Methods

Sample characterization. Single crystals of $(Bi,Pb)_{2.12}Sr_{1.88}CuO_{6+\delta}$ were grown by the travelling solvent floating zone method. The sample growth and characterization methods have been reported previously[48]. The as-grown single crystals with nominal composition $Pb_{0.25}Bi_{1.87}Sr_{1.88}CuO_{6+\delta}$ were post-annealed in different atmospheres, including vacuum and high-pressure oxygen at different temperatures (500 °C∼600 °C) in order to adjust the doping level to change T_c and to make the samples homogeneous. Supplementary Fig. 1 shows the temperature dependence of magnetization for as-grown Bi2201 single crystals and for samples after various annealing processes. The as-grown OD5K showed a broad transition width of more than 3 K. After annealing, the magnetization of OD17K and OD11K showed a sharp transition width of approximately 1K. The OD0K showed no superconducting transition down to 2 K, which was the minimum temperature of our apparatus, thus we indexed it as OD0K.

ARPES measurements. The ARPES measurements were carried out on the angle-resolved photoemission system with a Helium discharge lamp in the Institute of Physics, Chinese Academy of Sciences, in Beijing, China. The photon energy was 21.218 eV, and the energy and angular resolution were set to 10 meV and 0.3 degree, respectively. The samples were cleaved in situ and measured under ultrahigh vacuum at a pressure lower than 6×10^{-11} mbar. The Fermi level was referenced by measuring on the Fermi edge of clean polycrystalline gold that was electrically connected to the sample.

RIXS and RXS measurements. The RIXS measurements were performed at the ID32 beamline of ESRF (The European Synchrotron, Grenoble, France) using the high-resolution ERIXS spectrometer. The resonant conditions were achieved by tuning the energy of the incident X-rays to the maximum of the Cu L_3 absorption peak, around 931 eV. The total instrumental energy resolution was set at 65 meV, determined as the full-width at half-maximum of the non-resonant diffuse scattering from the silver paint. The samples were cleaved out-of-vacuum to expose a fresh surface. The XAS measurements were made at the ID32 beamline of ESRF. The RIXS experimental geometry is shown in Supplementary Fig. 5. X-rays are incident on the sample surface and scattered by an angle 2θ. Reciprocal lattice units (r.l.u.) were defined by using the pseudo-tetragonal unit cell with $a=b=3.83$ Å and $c=24.54$ Å, where the axis c is normal to the cleaved sample surface. The sample can be rotated azimuthally around the c axis to choose the in-plane wavevector component. Data in the text were taken with $2\theta=149°$, giving $|\mathbf{Q}|=0.85$ Å^{-1}, which allows one to cover the whole first Brillouin zone along the [100] direction (∼0.82 Å^{-1}). Here, the negative (positive) $Q_{\parallel}$ corresponds to grazing-incidence (grazing-emission) geometry. For Q_{CO}∼0.09–0.14 r.l.u., the L values correspond to 3.5–3.44 r.l.u.. Each RIXS spectrum was measured for 1 minute (sum of individual spectra of 5 seconds). The quasi-elastic intensity was determined by the integral of 0 ± 0.1 eV. That intensity was normalized to the integral of dd excitations in the RIXS spectrum between 1 and 3 eV energy loss. For the polarimeter measurements, the spectrum without polarimeter was measured for 15 min and the spectrum with polarimeter was measured for 50 min. The total instrumental energy resolution was set at ∼100 meV. The integrated intensity of the REXS peak is proportional to $\xi_H^{-1}\varsigma_H^{-1}d$, where d is the height of the REXS peak after subtracting the background from the curves of Fig. 2b.

The energy-integrated resonant X-ray scattering (RXS) measurements were performed at the UE46-PGM1 beamline at the BESSY II synchrotron of the Helmholtz-Zentrum-Berlin, Germany. The geometry was identical to that of the RIXS experiment. We used linearly polarized incident light perpendicular to the scattering plane (σ-polarization). The sample was mounted inside an ultrahigh-vacuum two-circle diffractometer and directly onto the cold finger of a liquid-Helium-flow cryostat, allowing a lower base temperature (∼10 K) than the RIXS set-up and, thus, measurements below T_c for the OD17K sample. The scattered photons were detected using a standard photodiode without discrimination of either polarization and energy, implying that the measured intensities represent an integration over all elastic and inelastic scattering processes.

The theoretical model and calculations. Our theoretical approach is based on a Fermi liquid scheme (details in Supplementary Information), which is the standard description of the metallic state. In this framework, the effects of CO with wavevector $\mathbf{Q}_{co}$ are described by the charge susceptibility in the customary random phase approximation (RPA). A charge instability at a given wavevector $\mathbf{Q}_{co}$ is obtained by a diverging charge susceptibility. The instability conditions are realized by a large density of states (DOS) in two different regimes of the phase diagram: while in the overdoped region the strong vHs directly provides the required large DOS, below optimal doping the substantial electron–electron correlation raises the effective electron mass m^* and, consequently, the quasiparticle DOS (ref. [49]). Therefore, the bare single-particle susceptibility given by the Lindhard polarization function does not provide the instability conditions at its peak value. The above description of the CO instability has a mean-field character and it does not include the effect of the CO fluctuations. These are then considered within a standard Ginzburg–Landau approach describing the effects of fluctuations in spoiling the long-range CO state and leaving the CO with a finite correlation length.

Data availability. The data that support the findings of this study are available from the corresponding authors upon reasonable request.

References

48. Zhao, L. et al. High-quality large-sized single crystals of Pb-doped $Bi_2Sr_2CuO_{6+\delta}$ high-T_c superconductors grown with traveling solvent floating zone method. *Chin. Phys. Lett.* **27**, 087401 (2010).
49. Kotliar, G. & Ruckenstein, A. E. New functional integral approach to strongly correlated Fermi systems: The Gutzwiller approximation as a saddle point. *Phys. Rev. Lett.* **57**, 1362–1365 (1986).